Article

Self-Healing Originated van der Waals Homojunctions with Strong Interlayer Coupling for High-Performance Photodiodes

Xiankun Zhang, Qingliang Liao, Zhuo Kang, Baishan Liu, Yang Ou, Junli Du, Jiankun Xiao, Li Gao, Hangyong Shan, Yang Luo, Zheyu Fang, Pengdong Wang, Zhe Sun, Zheng Zhang, and Yue Zhang

ACS Nano, **Just Accepted Manuscript** • DOI: 10.1021/acsnano.8b09130 • Publication Date (Web): 25 Feb 2019

is published by the American Chemical Society. 1155 Sixteenth Street N.W., Washington, DC 20036

Self-Healing Originated van der Waals Homojunctions with Strong Interlayer Coupling for High-Performance Photodiodes

Xiankun Zhang,[†] Qingliang Liao,[†] Zhuo Kang,[†] Baishan Liu,[†] Yang Ou,[†] Junli Du,[†] Jiankun Xiao,[†] Li Gao,[†] Hangyong Shan,[‡] Yang Luo,[‡] Zheyu Fang,[‡] Pengdong Wang,[§] Zhe Sun,[§] Zheng Zhang,[†,∥,*] Yue Zhang[†,∥,*]

[†]State Key Laboratory for Advanced Metals and Materials, School of Materials Science and Engineering, University of Science and Technology Beijing, Beijing 100083, People's Republic of China

[‡] School of Physics, State Key Laboratory for Mesoscopic Physics, Collaborative Innovation Center of Quantum Matter, Peking University, Beijing 100871, China

[§] National Synchrotron Radiation Laboratory, University of Science and Technology of China, Hefei, Anhui 230029, China

[∥] Beijing Municipal Key Laboratory for Advanced Energy Materials and Technologies, University of Science and Technology Beijing, Beijing 100083, People's Republic of China

KEYWORDS: *van der Waals homojunction; strong interlayer coupling; interface charge transfer; high responsivity and air-stability; defect self-healing*

ABSTRACT

The dangling-bond-free surfaces of van der Waals (vdW) materials make it possible to build ultrathin junctions. Fundamentally, the interfacial phenomena and related optoelectronic properties of vdW junctions are modulated by the interlayer coupling effect. However, the weak interlayer coupling of vdW heterostructures limits the interlayer charge transfer efficiency, resulting in low photo-responsivity. Here, a bilayer MoS_2 homogenous junction is constructed by stacking the as-grown onto the self-healed monolayer MoS_2. The homojunction barrier of ~165 meV is obtained by the electronic structure modulation of defect self-healing. This homojunction reveals the stronger interlayer coupling effect in comparison with vdW heterostructures. This ultra-strong interlayer coupling effect is experimentally verified by Raman spectrums and Angle resolved photoemission spectroscopy. The ultrafast interlayer charge transfer takes place within ~447 fs, which is faster than those of most vdW heterostructures. Furthermore, the homojunction photodiode manifests outstanding rectifying behavior with an ideal factor of ~1.6, perfect air-stability over 12 months, and high responsivity of ~54.6 mA/W. Moreover, the interlayer exciton peak of ~1.66 eV, are found in vdW homojunctions. This work offers an uncommon vdW junction with strong interlayer coupling and perfects the relevance of interlayer coupling and interlayer charge transfer.

Atomically thin and sharp van der Waals (vdW) heterostructures are fundamentally different from those made from conventional covalently bonded junctions.[1-3] Such unique structures have brought novel electronic and optoelectronic functionalities previously not possible in bulk materials.[4-6] Some vdW heterostructures behave strong light-matter interactions, photoluminescence (PL) quenching effect, and interlayer exciton emissions.[5, 7-12] However, the lattice mismatch of vdW heterointerface, which restraints are partially relaxed by dangling-bond-free surfaces, is still a non-negligible shortcoming also exists in new-generation heterostructures.[13-15] The interlayer couplings bonded by vdW forces are not enough to form strong interlayer coupling (lattice-matched) heterostructures, resulting in momentum mismatch and discontinuous band alignments.[3, 14, 16-21] Then, the interlayer charge transfer efficiency is limited to the degree assistance of external phonon, since momentum difference must be made up in interlayer movement.[22] Moreover, discontinuous band alignments, which originates from the energy band structure difference of lattice mismatch, can provoke substantial carrier scattering and trapping sites at heterointerfaces.[13, 20, 23, 24] Now, there is not still effective solutions to address lattice mismatch. Even epitaxial growth cannot completely solve this drawback and enhance the interface charge transfer efficiency.[3, 16, 25]

Conventional lattice-matched homojunctions are widely used in high-performance commercial optoelectronic devices because of their efficient interface charge transfer. Graphene,[26] MoS_2,[27-29] $MoTe_2$,[30-32] $MoSe_2$[13] and black phosphorus[33] two-dimensional (2D) homojunctions also manifest better-rectifying behavior and more efficient photoresponse than those of 2D vdW heterostructures. Nevertheless, the fundamental interlayer coupling mechanism is still rarely involved. An ideal homojunction study object is plagued by the poor control accuracy and instability of the homojunction processing technology (doping).[26, 29, 32] Still, defect engineering to control the electronic structure of monolayer MoS_2 behave high regulation precision and air-stability and have received much attention recently.[27, 34-38]

Here, the strong interlayer coupling vdW homojunctions are stacked by the two monolayer MoS_2 with different electronic structures *via* defects self-healing. Compared with vdW heterostructures, this homojunction exhibits stronger interlayer coupling effect. Meanwhile, the strong interlayer coupling effect at the lattice-matched interface can greatly enhance the interlayer charge transfer efficiency and promote the emergence of the photovoltaic effect. The ultrafast interlayer charge transfer takes place within ~447 fs, which is faster than those of most vdW heterostructures. Furthermore, the homojunction photodiode manifests outstanding rectifying behavior with an ideal factor of ~1.6, perfect air-stability over 12 months, and high responsivity of ~54.6 mA/W that greatly exceed those obtained for previous stacked or epitaxial heterobilayers. The observations compare the interlayer coupling differences between vdW heterostructures and vdW homojunctions, and provide the interlayer coupling damage mechanism about lattice mismatch for the preparation of high-performance 2D vdW structures.

RESULTS AND DISCUSSION

The stacked MoS_2 homojunction in Figure 1a was fabricated by artificial stacking of the as-grown (chemical vapor deposition, CVD) and self-healed MoS_2. The electronic structure regulation of the self-healed MoS_2 was completed by the as-mentioned poly(4-styrenesulfonate) (PSS)-induced sulfur vacancy self-healing (SVSH) effect. The self-healing mechanism is that the hydrogenation of PSS guides sulfur adatom clusters on the as-grown MoS_2 surface to heal sulfur vacancies (Figure S1, Supporting Information).[27] Figure 1b is the optical microscope image of a homojunction. As we all known, the electron concentration in less defective semiconductors is low and tends to its intrinsic electron concentration.[39, 40] To visually characterize the electron concentration change, the Kelvin probe force microscopy (KPFM) was performed. The KPFM image maps the variation of surface potential corresponding to the work function of the three typical domains in Figure 1c. The surface potential of the as-grown (blue), self-healed (red) and stacked (green) domains are ~195, ~30 and ~152 mV in Figure 1d, respectively. The deduced built-in potential barrier of the as-grown/self-healed homojunction is ~165 meV, which shows that the vdW homojunction has been successfully constructed through the self-healing.

The electronic structure regulation was reconfirmed. The absolute value of the threshold voltage in the self-healed MoS_2 transistor is much lower than those of the as-grown one (Figure 1e). This indicates that the native n-type doping in the as-grown monolayer was removed while the same drive voltage was maintained (Supporting Information Figure S2). To further confirm that the electronic structure regulation mainly originates from the self-healing, Auger electron spectroscopy (AES) was performed to prove the no fluctuation of sulfur atom content before and after self-healing (Supporting Information Figure S3). To sum up, the electronic structure control of the MoS_2 monolayers has been achieved by sulfur vacancy self-healing.

The PL spectrum intensity of the as-prepared homojunction is significantly stronger than that of the isolated monolayers in Figure 1f. The PL spectrum intensity of the stacked region is approximately equal to the intensity sum of the as-grown and self-healed MoS_2 (Supporting Information Figure S4). This phenomenon indicates that the as-prepared homojunction is lack of interlayer coupling. The stacked monolayers behave as if they are isolated from each other and exert the negligible fluctuation onto each other. In a word, the PL quenching effect of the homojunction seems not to work in this case, unlike vdW heterostructures.[10] However, after mild annealing at 250 ℃ for 9 h, the PL spectrum intensity of the stacked region decreased rapidly to less than that of the two monolayers in Figure 1g and 1h. Thus, the built-in electric field of the annealed MoS_2 homojunction can efficiently separate the photocarriers, and produce the PL quenching effect. This fundamental transformation could be attributed to the enhancement of the interlayer coupling strength of the MoS_2 vdW homojunction induced by mild annealing.

The Raman mapping in Figure 1i shows that the A_{1g} peak position is maintained before and after self-healing, and the peak intensities haven't changed significantly. Thus, the self-healing successfully regulates the electronic structure of MoS_2 monolayer, while also retaining its intrinsic properties. However, the peak position of the layer-sensitive A_{1g} mode for the annealed homojunction appears blue shift in Figure

1j. This suggests the interface vdW force between the as-grown and self-healed MoS_2 gradually work. The difference between the three kinds of E^1_{2g} peaks will be discussed in detail later. The frequency difference between the E^1_{2g} and A_{1g} Raman modes in the stacked region was increased to ~22.1 cm^{-1} by the mild annealing (Figure 1j). The value is larger than that of the isolated monolayers (~19.7 and ~21.0 cm^{-1}) and consistent with that of the natural bilayer MoS_2 (22-24 cm^{-1}). This reflects that the coupling strength is enhanced close to that of natural bilayer by mild annealing.[41]

To reduce the effect of thermal excitation of phonons on the interlayer excitons stability, the low-temperature PL spectrum characterization was performed. Compared to the as-mentioned PL spectrums at room temperature, these PL spectrums of the homojunction exhibit three differences in Figure 2a and Supporting Information Figure S5. Firstly, a new PL peak of ~1.74 eV appears in the as-grown monolayer and stacked homojunction but not in the self-healed sample. This peak is a defect peak X_D closely related to the sulfur vacancies of the as-grown MoS_2.[42, 43] Secondly, the A peak of the homojunction is resolved into the sum of those of the as-grown and self-healed monolayer. Thus, the intralayer A peaks of the isolated MoS_2 monolayers coexist in the stacked region, which demonstrates the preservation of intralayer excitons in the homojunction. The homojunction also contains the defect peak X_D of the as-grown monolayer, which again indicates that there is some independence of the isolated monolayers in the strongly coupled homojunctions.

Last and most important, the interlayer coupling also creates the radiative recombination of interlayer excitons of X_I (~1.66 eV), which is experimentally observed in vdW homojunctions. The reason for not observing X_I at room temperature may be that increasing the temperature decreases the PL spectrum intensity of the interlayer exciton.[44] Since X_I has never been observed in the as-grown and self-healed samples, the origin of X_I should not come from the two isolated monolayers. Under the same measurement environments, no similar peaks about interlayer excitons of X_I are observed in the as-grown/as-grown homobilayer (Supporting Information Figure S6).

Ultraviolet photoelectron spectroscopy (UPS) was implemented to further confirm the origin of X_I. In Figure 2b, the energy difference between the Fermi level and valence band maximum (Δ_{VB}) is decreased from ~1.76 to ~1.53 eV, demonstrating the electron concentration decrease of monolayer MoS_2. Thus, the difference of the Δ_{VB} between the as-grown and self-healed film is ~0.23 eV. After our self-healing, the work function of MoS_2 monolayer has also increased from ~4.43 to ~4.62 eV in Figure 2c. In addition, the work function difference between the as-grown and self-healed monolayers is ~0.19 eV, which was close to ~0.16 eV obtained by as-mentioned KPFM measurement in Figure 1c. The interlayer exciton peak X_I (~1.66 eV) observed in Figure 2a is approximately equal to the energy difference (~1.63 eV) between X_A and Δ_{VB}. This indicates that the interlayer excitons are composed of electrons and holes provided by the as-grown and self-healed samples, respectively. On the other hand, the binding energy of interlayer excitons is often negatively related to the degree of formation difficulty. The electronic energy bandgap of the less defective and more defective monolayers are ~2.61 and ~2.34 eV.[45] Then, the binding energy (~0.45 eV) of the interlayer excitons deduced is less than the intralayer excitons of the isolated monolayers (~0.69 and ~0.48 eV) in Figure 2d.

The transient absorption measurements were used to further monitor the carrier and exciton dynamics of the MoS_2 homojunction. The fast time constants (~378, ~168 and ~447 fs) is associated with photocarrier lifetime in Figure 2e.[15, 46] The time constant comparison of the as-grown, self-healed and homojunction shows clearly the interlayer photocarrier transfer occurs in the interface between the two MoS_2 monolayers. With no efficient interlayer transfer, the decay signal of the homojunction would show as a simple sum of the as-grown and self-healed MoS_2. Or, the signal would be dominated by the recombination of carriers in the as-grown monolayer on the larger time scale of ~378 fs. However, the sum of the reflection delay signal of two separated monolayers is obviously different from those of the homojunction (Figure 2f). This proves that the interlayer charge transfer takes place in Figure 2g, driven by the potential barrier between the self-healed and as-grown monolayers.

The electron transfer from the self-healed to as-grown takes place within ~447 fs, which is significantly faster than those of most vdW heterostructures.[7, 15] Due to the effect of momentum mismatch between the adjacent layers of vdW heterostructures, the rates of photocarrier transfer and recombination depend on the magnitude of phonons assistance.[11, 15, 18, 22] With no momentum mismatch, the interlayer charge transfer of vdW homojunctions does not require phonon assistance. Besides, heterostructures do not have continuous band alignments and contain the cusp and notch between the conduction and valence bands. Those drawbacks could provoke carrier scattering and trapping sites to decrease the interlayer transfer efficiency.[20, 23]

Figure 3a is the structure diagram and OM image of the MoS_2 homojunction photodiode. In Figure 3b， the two types of homojunctions show good current rectification performance which is further quantitatively analyzed under bias voltage by fitting to the diode equation[47-49]

$$I_D = I_S\left[\exp\left(\frac{V_D}{nV_T}\right) - 1\right], \quad (2)$$

where I_S, n and V_T denote reverse bias saturation current, the ideality factor, and thermal voltage, respectively. Thus, n can be calculated from linearly fitting the natural logarithm plot of current and voltage. The ideal factor n and the rectifying ratio of the MoS_2 homojunction are ~1.6 and ~72, respectively. This ideality factor is much better than heterostructures p-n diodes in bulk semiconductors or 2D materials ($n >> 2$), which can be attributed to the continuous band alignment and fewer carrier traps of the homojunction interface.[13, 20, 28, 32, 50] On the other hand, unlike unstable conventional doping effects, this current rectifying performance is able to remain unchanged under atmosphere for 12 months in Figure 3c. To confirm that the origin of the rectifying behavior, the electrical transport properties of other contact types were characterized. Ohmic characteristics are all obtained among the following two types of contact (Supporting Information Figure S2 and S7): the as-grown or self-healed MoS_2 and Au electrodes. So, the existence possibility of large potential barrier in electrode contact interfaces is excluded. In addition, the linear output curve of the as-grown/as-grown MoS_2 homobilayer suggests the self-healed sample is the key component of the rectifying effect (Supporting Information Figure S7). Thus, the current rectifying behavior of the MoS_2 homojunction originates from its interlayer potential barrier between the as-grown and self-healed MoS_2.

In fact, the rectifying behavior of the MoS_2 homojunction diode can be regulated by an external electric field. When the gate voltage changes from negative to positive, the rectifying ratio of the MoS_2 homojunction is gradually reduced to close to 1 in Figure 3d-e. When the vertical upward electric field produced by positive gate voltage is sufficiently large, the original built-in electric field of the homojunction will be almost eliminated in Figure 3f. The built-in electric field of the MoS_2 homojunction and the electric field generated by gate voltage can be calculated $E= U/(\varepsilon_r \mathrm{d})$. The built-in potential U, interlayer vacuum gap d and vacuum relative permittivity ε_r are 165 mV, 0.35 nm and 1 respectively. The gate voltage of the rectifying ratio of ~1 is 90 V, the thickness and relative permittivity of the SiO_2 insulating layer are 300 nm and 3.9 respectively. The electric field of ~1.17 V/nm generated by gate voltage is close to the built-in electric field of ~0.47 V/nm, which shows that the change of the rectifying ratio mainly comes from the variation of the built-in electric field. Unlike vdW homojunctions, it is almost impossible to regulate the rectifying junction of similar vdW heterostructures as an ohmic junction.[11] Because the bandgaps of two adjacent monolayers of vdW heterostructures are different and their abilities controlled by gate voltage are also different.

We also investigated the photoresponse of the as-prepared homojunction, but no photovoltaic effect was observed in Figure 4a. However, after complete mild annealing, the annealed homojunction exhibit a photovoltaic effect with the open-circuit voltage of ~70 mV and short-circuit current of ~1.1 nA in Figure 4b. This fundamental shift can be attributed to that mild annealing removes the limitations that impede the photocarrier separation in Figure 4c. The same annealing process was also applied to the as-grown/as-grown MoS_2 homobilayer. The linear output curve still exists (Supporting Information Figure S7). Moreover, no photovoltaic effect is discovered in Figure 4d. These results again demonstrate that the built-in potential barrier is an essential component of forming the current rectifying effect and photovoltaic effect. This photovoltaic effect confirms that interlayer charge transfer can occur in the MoS_2 homojunction, which is also consistent with the PL quenching effect and the prolongation of the carrier lifetime.

The light responsivity of the MoS_2 photodiode is negatively correlated with laser intensity, up to ~54.6 mA/W at zero biased voltage in Figure 4e. Corresponding external quantum efficiency (EQE) reaches 12.8%, which performance greatly exceed those obtained for previous stacked or epitaxial heterobilayers (Supporting Information Table S1).[1, 2, 11, 26, 39, 51, 52] The above results show that enhancing the interlayer coupling strength is an effective way to improve the interlayer charge transfer. In addition, the rise time (0–90%) and recovery time (10–100%) are ~3.10 and ~0.38 s, respectively in Figure 4f. The response speed is much faster than that of many 2D materials-based photodiodes.

As all we known, gradually reducing the interlayer gap can make the coupling effect of interlayer vdW force increase exponentially.[6] The transformation mechanism we proposed is that mild annealing can remove interlayer residues and thus reduce the interlayer gap in Figure 5a. The interlayer gap can be attributed to the unexpected residues (water, ambient gas and speckles) trapped at the interface during the transfer process.[53, 54] Figure 5b shows that the as-prepared homojunction has an interlayer step of ~2.5 nm significantly larger than its expected equilibrium value (monolayer MoS_2 thickness, 0.65 nm) (Supporting Information Figure S8). This interlayer step was reduced from ~2.5 nm to ~1.0 nm by the complete annealing.

To simply compare the photocarrier separation efficiency at different coupling strength in Figure 5c, the PL spectrum intensity ratio between the homojunction (I_H) PL spectrum intensity and the PL spectrum intensities sum of the as-grown (I_A) and self-healed (I_S) MoS_2 is normalized by the value that is, $R = I_H / (I_A + I_S)$. With the increase of the annealing time, the PL spectrum intensity ratio R decreases gradually from 0.94 to 0.23, and the photocarrier separation efficiency grows gradually which indicates that the interlayer coupling strength of the homojunction raises. Due to no potential difference in the adjacent monolayers of the as-grown/as-grown homobilayer (Supporting Information Figure S9), the interlayer charge transfer effect can be ignored.[11, 46] In addition, self-healing makes both the A and B exciton resonances of the as-grown monolayer clearly blue-shifted. The amounts of change are consistent with those of the absorption spectrums (Supporting Information Figure S10), which indicates self-healing has successfully regulated the electronic structure of the as-grown monolayer.

As the annealing time increases in Figure 5d and 1j, the peak position of the layer-sensitive A_{1g} mode for the homojunction appears blue shift, which suggests the interface vdW force between the as-grown and self-healed MoS_2 gradually work. When the interlayer step decreases, the interlayer vdW force in the homojunction suppresses atom vibration, resulting in the high force constants. A_{1g} modes are supposed to stiffen (blue-shift). The frequency difference between A_{1g} and E^1_{2g} peak in the homojunction and homobilayer is consistent with that of the exfoliated bilayer MoS_2 in Figure 5e. This result reflects that the coupling strength is enhanced close to that of exfoliated bilayer by mild annealing.

The strong interlayer coupling of the MoS_2 homojunction not only acts on the vertical vibration of the S-Mo bond but also changes its horizontal vibration. As the annealing time increases, the in-plane E^1_{2g} peak of the homojunction has been gradually merged from the two superimposed peaks into an individual peak. Figure 5d and 1j show that the difference between the E^1_{2g} peaks of the as-grown and self-healed films is due to the wrench of the S-Mo bond and the lateral stretching of sulfur atoms induced by the sulfur vacancies.[55] The in-plane E^1_{2g} peak will be divided into two since the anomalous splitting of the degenerate interlayer shear phonon modes by uniaxial strain or plasma treatment.[45, 56, 57] Therefore, the strong interlayer coupling effect can bind two irrelevant monolayers together.

In the following, Low-frequency (LF) interlayer Raman modes were used to further study the annealing enhanced interlayer coupling mechanism in Figure 5f. The difference between LF and high-frequency (HF) Raman modes is detailed in Supporting Information Figure S11.[58] In Figure 5f, a pronounced Raman peak layer-breathing mode (LBM) emerges at ~35.8 cm^{-1} for the 1 h annealed MoS_2 homojunction. This

Raman feature isn't observed in the two isolated monolayers, indicating that mild annealing improves the interlayer interaction. Then, the LBM vibrational frequency of the 9 h annealed homojunction increased from ~35.8 to ~38.5 cm^{-1}, which is very close to ~41 cm^{-1} of the mechanically exfoliated bilayer MoS_2.[58] In vdW structures, greater LBM frequency means stronger interlayer coupling strength.[59] The LBM frequencies of vdW heterostructures are relatively small and only 30-35 cm^{-1}.[58, 59] Thus, prolonging the annealing time can improve the interlayer coupling strength. Simultaneously, the MoS_2 vdW homojunction possesses stronger interlayer coupling strength than vdW heterostructures.

Shear mode (SM) vibrations are different from LBM vibrations. Only when the two layers have high-symmetry (2H) stacking are SM modes active since the lateral displacement can provide the restoring forces (Supporting Information Figure S11). After mild annealing for 9 hours, the SM peak of ~22.5 cm^{-1} finally appears in Figure 5f, which indicates that the annealed homojunction is a vdW structure with the lattice-matched coherent region. Due to lattice mismatch between the two layers, vdW heterostructures are almost impossible to form lattice-matched structures; even it is of epitaxial growth.[3, 14, 16, 58] After the same complete annealing, the MoS_2/WS_2 heterostructure does not appear SM peaks, indicating that the lattice-matched coherent junction still doesn't forms (Table 1 and Supporting Information Figure S12). SM peaks have barely been detected in other vdW heterostructures.[22]

Our discovery indicates that the highly efficient interlayer charge transfer of homojunctions are attributed to strong interlayer coupling compared to vdW heterostructures. To compare farther the interlayer coupling strength between vdW homojunctions and heterostructures, angle-resolved photoemission spectroscopic (ARPES) experiments and density functional theory (DFT) calculations were carried out. The homojunction has been proved to have greater interlayer coupling strength than most vdW heterostructures and are indirect bandgap junctions (Table 1, Figure 6 and Supporting Information Figure S13-14). The valence band maximum (VBM) of the MoS_2 homojunction is at Γ point (Figure 6). Whereas, the VBM of MoS_2 monolayer is at K point in Figure 6b. For MoS_2 homojunction, the band edge near K will almost not move before and after stacking for their Mo-d_{xy} and Mo-$d_{x^2-y^2}$ states are localized within the adjacent layers. While the valence state at the Γ point has appreciable S-p_z content between layers, as well as Mo-d_{z^2} character. In short, the VBM of Γ point is very sensitive to interlayer interactions, and the VBM of K point is almost unaffected by interlayer coupling strength. The resulting band structures mostly depend on the interlayer coupling strength.[21, 60] Therefore, the strong interlayer orbital hybridization exists in the stacked MoS_2 homojunctions. In addition, the interlayer coupling strength of MoS_2 homojunction is much higher than that of similar vdW heterostructures (Supporting Information Figure S14). Although the MoS_2 homojunction is an indirect band gap in Figure 6c, the defect energy levels of the sulfur vacancies hinder the indirect exciton observation (Supporting Information Figure S15).

However, there is no indirect exciton peak observed in the as-grown/self-healed MoS_2 homojunction in Figure 6c. Meanwhile, no indirect exciton peak is observed in the as-grown/as-grown MoS_2 commensurate homobilayer. More interestingly, after some sulfur vacancies were made in the top monolayer of the exfoliated MoS_2 bilayer by hydrogen annealing, the original indirect exciton peak disappeared (Supporting Information Figure S15). Thus, sulfur vacancies in MoS_2 homojunctions or commensurate homobilayers have a very negative effect on the formation of indirect (K-Γ) exciton peaks. The deep and shallow states created by sulfur vacancies may prevent the recombination of electrons from K point and holes from Γ point (Supporting Information Figure S13). Deeper influence mechanism is still not clear yet to be further explored.

CONCLUSIONS

In summary, a bilayer MoS_2 homogenous junction was constructed by stacking the as-grown onto the self-healed monolayer MoS_2. The interlayer coupling of the vdW homojunction is experimentally proved to be stronger than that of reported vdW heterostructures. The homojunction photodiode manifests outstanding rectifying behavior of ideal factor of ~1.6, perfect air-stability of 12 months and high responsivity of ~54.6 mA/W that greatly exceed those obtained for previous stacked or epitaxial heterobilayers. The ultrafast interlayer charge transfer takes place within ~447 fs, resulting in the drastic PL quenching effect and photovoltaic effect. Our results compare the interlayer coupling differences between vdW heterostructures and vdW homojunctions, offer a fresh idea to design and optimal vdW structures to enhance the interlayer charge transfer efficiency, and provide a global understanding of the interlayer coupling damage mechanism about lattice mismatch.

MATERIALS AND METHODS

Growth of monolayer MoS_2. The MoS_2 monolayers were grown at 850 °C for 30 min onto SiO_2/Si substrates by the oxygen-assisted chemical vapor deposition (CVD) method.[61] MoO_3 (Sigma-Aldrich, ≥ 99.5% purity) and sulfur (Sigma-Aldrich, ≥99.5% purity) were applied as precursor and reactant materials respectively. MoO_3 powder (25 mg) was placed in a quartz boat at the center of the furnace. A 2 × 2 cm^2 SiO_2/Si substrates were put face down at top of the MoO_3 powder. Excessive S powder was heated to 180 ℃ by the heating belt and carried through Ar flow of 500 sccm. The experiments were implemented at a reaction temperature of 850 ℃ for 30 min with oxygen assistance of 2 sccm. It needs to point out that the sample cooling process was carried out in the sulfur vapor at 180 ℃. Thus, a large number of sulfur clusters will be stationed on MoS_2 monolayers surface.

Construction of the as-grown/self-healed MoS_2 homojunctions and the as-grown/as-grown homobilayers. The as-grown/self-healed homojunctions were prepared using standard PMMA-based transfer as below. Firstly, the CVD grown MoS_2 was immersed in the poly(3,4ethylenedioxythiophene):poly(4-styrenesulfonate) (PEDOT:PSS) solution (Sigma-Aldrich, 1.0 wt%), after standing for 1 h, and then immersed in plenty of DI water at 120 ℃ to totally wash the PEDOT:PSS solution for 30 min. Secondly, PMMA was spin-coated on as-grown monolayer MoS_2 and warmed at 120 °C for >2 min. The PMMA/MoS_2 sample was separated from the SiO_2/Si substrate by mildly etching SiO_2 in 1 mol/L KOH solution for 0.5-2 h. The

PMMA/MoS_2 sample was transferred to DI water to reduce KOH residue. Then, with the aid of accurate transfer platform (Metatest, E1-T), the as-prepared film was transferred onto the self-healed MoS_2 on SiO_2/Si substrate. One of the criteria in the stacking process is that the twist angle should be as close to 0° or 60° as possible. Due to the smaller interlayer gap, the interlayer coupling strength is particularly strong at this moment.[41, 62] The PMMA layer was removed by acetone and then rinsed with isopropyl alcohol. Thirdly, mild vacuum annealing of several hours at 250 ℃ was used to increase the interlayer adhesion between the as-grown and self-healed monolayers. The construction of the homobilayer removes the solution treatment step, and the rest of the process is similar to those of the homojunction.

KPFM measurement. To visually characterize the electron concentration change, a Kelvin probe force microscopy (KPFM) was employed to verify the work function variation of MoS_2 nanosheets. The contact potential difference (CPD) between the AFM tip (Pt/Ir coated tips) and the sample is defined as[63-65]

$$V_{CPD} = \frac{\varphi_{\mathrm{sample}} - \varphi_{tip}}{q},$$

where φ_{sample}, φ_{tip} and q are the work functions of the sample, tip and the elementary charge, respectively.

UPS measurement. The work function variation of the monolayer MoS_2 was also carefully double-checked by UPS which is used to explore the energy level alignment with respect to the Fermi energy (E_F). The as-grown and self-healed MoS_2 are separately transferred onto Si substrates coated with 70 nm thermally evaporated Au. The Au layer serves as a reference for E_F, assigned to 0 eV. The work function can be calculated using[66]

$$\phi = h\nu - E_{onset},$$

where $h\nu$ is the incident photon energy (21.22 eV) and E_{onset} is the onset level related to the secondary electrons. Then, the energy difference between the Fermi level and valence band maximum is decreased from 1.76 to 1.53 eV, demonstrating the electron concentration decrease of monolayer MoS_2. The calculated difference of the valence band maximum Δ_{VB} between the as-grown and self-healed film is ~0.23 eV. Hence, the ϕ for the as-grown and self-healed MoS_2 is 4.43 and 4.62 eV, respectively.

Transient absorption measurements. The time-resolved differential reflection is defined as $\Delta R/R_0 = (R - R_0)/R_0$, where R and R_0 are the reflectivity of the probe with and without the presence of the pump, respectively. The decay signals of the three regions are fitted by biexponential function ($\Delta R/R_0 = A_1 e^{-t/\tau 1} + A_2 e^{-t/\tau 2} + B$) with fast ($\tau_1$) and slow ($\tau_2$) decay components. The slow time constants (~6.1, ~3.1 and ~10.5 ps) are attributed to the defect-mediated electron-hole recombination. This difference between the homojunction and the isolated monolayers indicates that although annealing minimizes the adverse effects of the residues in the interface, the few residues are still involved into the capture and release of photocarriers. The prolongation of the slow time constants is related to the recombination of electron-hole pairs dominated by defects *via* Auger processes.[67, 68] The recombination rate will be significantly reduced.

Sulfur vacancies also have similar functions as the interface residues. Thus, the as-grown one (~6.1 ps) has a time scale much longer than that of the self-healed MoS_2 (~3.1 ps). Similar enhancement of carrier lifetime has also been observed in the exfoliated MoS_2 monolayer with and without high-power laser-induced defects.[67]

ARPES measurement. The as-prepared MoS_2 homojunction was transferred to the silicon substrates by standard PMMA-based transfer. Fresh surfaces were obtained by monocrystalline MoS_2 film samples annealed at 300 ℃ in a vacuum chamber for two hours. Samples were under a base pressure of 5×10^{-11} mbar and cooled to 30 K with liquid helium during measurements. The main ARPES measurements were performed at the 'Dreamline' beamline of the Shanghai Synchrotron Radiation Facility (SSRF) with a Scienta Omicron DA30L analyser. The photon energy ranged from 70 eV to 200 eV. The energy resolution was 25 meV, and the angular resolution was 0.1°.

DFT Calculations. The calculation was performed using the projector augment wave methods[69] as implemented in the Vienna *Ab initio* Simulation Package (VASP) within the generalized gradient approximation[70] and the spin-orbit interaction is included. The cutoff energy of the plane-wave was set to 600 eV. The first Brillouin zone is sampled on a $24 \times 24 \times 1$ k-point Gamma centered mesh for the density optimizations. During structural relaxation, the energy convergent criterion was 10^{-5} eV per unit cell, and the forces on all relaxed atoms were less than 0.03 eVÅ^{-1}. A vacuum layer of more than 20 Å was used to decouple the adjacent atomic slabs between the neighboring supercells.

Measurements. The KPFM and AFM measurements were taken on a commercially available AFM (Nanoscope IIID, Multimode). Scanning electron microscopy (SEM) observation was done in an FEI Quanta 3D. The PL and Raman spectrum measurements were performed with confocal microscopy (JY-HR800 and WITec CRM200) excitation under 532 nm laser with a power of 20 mW. The spot size of the laser is about 1 μm^2. The step size for Raman and PL map is about 0.1-0.5 μm. The variable temperature PL spectrums were characterized in Renishaw inVia plus. UPS curves were obtained in an ultrahigh vacuum chamber using a helium lamp source emitting (AXIS ULTRA DLD) at 21.2eV. The pump-probe measurements were measured by a home-built platform with a mode-locked oscillator (Tsunami 3941C-25XP), photonic crystal fiber (Newport SCG-800) and a high-sensitivity photomultiplier (Thorlabs PMM02). The photocurrent used 532 nm laser as light source. The electrical characteristics and the photoresponse properties were implemented by a semiconductor analysis system (Keithley 4200). All electrical and optical signals were recorded in the ambient atmosphere, except variable temperature PL spectrums.

ASSOCIATED CONTENT

*Supporting Information

The Supporting Information is available free of charge on the ACS Publications website at DOI: xxxxx.

Figures S1-S15, Table S1, and references (refs 1-3). Additional discussion on AES measurement, absorption spectra, interlayer gap, detailed low-temperature PL spectrums and further characterization of interlayer exciton peaks (PDF).

Conflict of Interest: The authors declare no competing financial interest.

AUTHOR INFORMATION

Corresponding Author

*E-mail: zhangzheng@ustb.edu.cn;

*E-mail: yuezhang@ustb.edu.cn.

ORCID

Zheng Zhang: 0000-0002-9104-7562

Yue Zhang: 0000-0002-8213-1420

Author Contributions

X.K.Z, L.G. and B.S.L deposited MoS_2 films by CVD. X.K.Z. and Z.Z. performed the device fabrication, data collection and analysis. Q.L.L., J.L.D and L.G. assisted in carrying out the film fabrication and characterizations. J.K.X. and L.G. assisted in the device performance measurements. J.L.D and X.K.Z carried out KPFM and AFM measurements. X.K.Z., Z.K. and B.S.L performed part of the Raman, PL and UPS characterization. Y.O. and Z.Z. completed the theoretical calculation part. Y.L., H.Y.S. and Z.Y.F. are responsible for the absorption spectra and transient absorption measurements. B.D.W. and Z.S. are in charge of the ARPES measurements. Z.Z. and

Y.Z. initiated and supervised the project. All authors have given approval to the final version of the manuscript. †X.K.Z. and Q.L.L. contributed equally.

ACKNOWLEDGMENTS

This work was supported by the National Natural Science Foundation of China (No. 51527802, 51602020, 51722203, 51672026, 11674012， U1532136), the Overseas Expertise Introduction Projects for Discipline Innovation (No. B14003), the Beijing Natural Science Foundation (Z180011), National Key Research and Development Program of China (No. 2016YFA0202701), the Fundamental Research Funds for the Central Universities. ARPES data were acquired at the beamline 09U (dreamline) in Shanghai Synchrotron Radiation Facility (SSRF) and beamline 13U in National Synchrotron Radiation Laboratory (NSRL).

REFERENCES

1. Liu, Y.; Weiss, N. O.; Duan, X.; Cheng, H.-C.; Huang, Y.; Duan, X., Van der Waals Heterostructures and Devices. *Nat. Rev. Mater.* **2016**, 1, 16042.
2. Novoselov, K. S.; Mishchenko, A.; Carvalho, A.; Castro Neto, A. H., 2D Materials and van der Waals Heterostructures. *Science* **2016**, 353, aac9439.
3. Lotsch, B. V., Vertical 2D Heterostructures. *Annu. Rev. Mater. Res.* **2015**, 45, 85-109.
4. Frisenda, R.; Molina-Mendoza, A. J.; Mueller, T.; Castellanos-Gomez, A.; van der Zant, H. S. J., Atomically Thin p-n Junctions Based on Two-Dimensional Materials. *Chem. Soc. Rev.* **2018**, 47, 3339-3358.
5. Jin, C.; Ma, E. Y.; Karni, O.; Regan, E. C.; Wang, F.; Heinz, T. F., Ultrafast Dynamics in van der Waals Heterostructures. *Nat. Nanotechnol.* **2018**, 13, 994-1003.
6. Song, J. C. W.; Gabor, N. M., Electron Quantum Metamaterials in van der Waals Heterostructures. *Nat. Nanotechnol.* **2018**, 13, 986-993.
7. Ceballos, F.; Bellus, M. Z.; Chiu, H.-Y.; Zhao, H., Ultrafast Charge Separation and Indirect Exciton Formation in a MoS_2-$MoSe_2$ van der Waals Heterostructure. *ACS Nano* **2014**, 8, 12717-12724.
8. Hong, X.; Kim, J.; Shi, S.-F.; Zhang, Y.; Jin, C.; Sun, Y.; Tongay, S.; Wu, J.; Zhang, Y.; Wang, F., Ultrafast Charge Transfer in Atomically Thin MoS_2/WS_2 Heterostructures. *Nat. Nanotechnol.* **2014**, 9, 682-686.
9. Xu, W.; Liu, W.; Schmidt, J. F.; Zhao, W.; Lu, X.; Raab, T.; Diederichs, C.; Gao, W.; Seletskiy, D. V.; Xiong, Q., Correlated Fluorescence Blinking in Two-

Dimensional Semiconductor Heterostructures. *Nature* **2017**, 541, 62-67.

10. Fang, H.; Battaglia, C.; Carraro, C.; Nemsak, S.; Ozdol, B.; Kang, J. S.; Bechtel, H. A.; Desai, S. B.; Kronast, F.; Unal, A. A.; Conti, G.; Conlon, C.; Palsson, G. K.; Martin, M. C.; Minor, A. M.; Fadley, C. S.; Yablonovitch, E.; Maboudian, R.; Javey, A., Strong Interlayer Coupling in van der Waals Heterostructures Built from Single-Layer Chalcogenides. *Proc. Natl. Acad. Sci.* **2014**, 111, 6198-6202.
11. Lee, C. H.; Lee, G. H.; van der Zande, A. M.; Chen, W.; Li, Y.; Han, M.; Cui, X.; Arefe, G.; Nuckolls, C.; Heinz, T. F.; Guo, J.; Hone, J.; Kim, P., Atomically Thin p-n Junctions with van der Waals Heterointerfaces. *Nat. Nanotechnol.* **2014**, 9, 676-681.
12. Zhang, X.; Meng, F.; Christianson, J. R.; Arroyo-Torres, C.; Lukowski, M. A.; Liang, D.; Schmidt, J. R.; Jin, S., Vertical Heterostructures of Layered Metal Chalcogenides by van der Waals Epitaxy. *Nano Lett.* **2014**, 14, 3047-3054.
13. Jin, Y.; Keum, D. H.; An, S. J.; Kim, J.; Lee, H. S.; Lee, Y. H., A van der Waals Homojunction: Ideal p-n Diode Behavior in $MoSe_2$. *Adv. Mater.* **2015**, 27, 5534-5540.
14. Constantinescu, G. C.; Hine, N. D. M., Energy Landscape and Band-Structure Tuning in Realistic $MoS_2/MoSe_2$ Heterostructures. *Phys. Rev. B* **2015**, 91, 195416.
15. Chen, H.; Wen, X.; Zhang, J.; Wu, T.; Gong, Y.; Zhang, X.; Yuan, J.; Yi, C.; Lou, J.; Ajayan, P. M.; Zhuang, W.; Zhang, G.; Zheng, J., Ultrafast Formation of Interlayer Hot Excitons in Atomically Thin MoS_2/WS_2 Heterostructures. *Nat. Commun.* **2016**, 7, 12512.

16. Zhang, C.; Chuu, C.-P.; Ren, X.; Li, M.-Y.; Li, L.-J.; Jin, C.; Chou, M.-Y.; Shih, C.-K., Interlayer Couplings, Moiré Patterns, and 2D Electronic Superlattices in MoS_2/WSe_2 Hetero-Bilayers. *Sci. Adv.* **2017**, 3, e1601459.

17. Wang, Y.; Wang, Z.; Yao, W.; Liu, G.-B.; Yu, H., Interlayer Coupling in Commensurate and Incommensurate Bilayer Structures of Transition-Metal Dichalcogenides. *Phys. Rev. B* **2017**, 95, 115429.

18. Zhu, H.; Wang, J.; Gong, Z.; Kim, Y. D.; Hone, J.; Zhu, X. Y., Interfacial Charge Transfer Circumventing Momentum Mismatch at Two-Dimensional van der Waals Heterojunctions. *Nano Lett.* **2017**, 17, 3591-3598.

19. Liu, X.; Hersam, M. C., Interface Characterization and Control of 2D Materials and Heterostructures. *Adv. Mater.* **2018**, 30, e1801586.

20. Huang, X.; Liu, B.; Guan, J.; Miao, G.; Lin, Z.; An, Q.; Zhu, X.; Wang, W.; Guo, J., Realization of In-Plane p-n Junctions with Continuous Lattice of a Homogeneous Material. *Adv. Mater.* **2018**, 30, 1802065.

21. Wilson, N. R.; Nguyen, P. V.; Seyler, K.; Rivera, P.; Marsden, A. J.; Laker, Z. P.; Constantinescu, G. C.; Kandyba, V.; Barinov, A.; Hine, N. D., Determination of Band Offsets, Hybridization, and Exciton Binding in 2D Semiconductor Heterostructures. *Sci. Adv.* **2017**, 3, e1601832.

22. Kunstmann, J.; Mooshammer, F.; Nagler, P.; Chaves, A.; Stein, F.; Paradiso, N.; Plechinger, G.; Strunk, C.; Schüller, C.; Seifert, G., Momentum-Space Indirect Interlayer Excitons in Transition Metal Dichalcogenide van der Waals Heterostructures. *Nat. Phys.* **2018**, 14, 801-805.

23. Zhang, C.; Li, M. Y.; Tersoff, J.; Han, Y.; Su, Y.; Li, L. J.; Muller, D. A.; Shih, C. K., Strain Distributions and Their Influence on Electronic Structures of WSe_2-MoS_2 Laterally Strained Heterojunctions. *Nat. Nanotechnol.* **2018**, 13, 152-158.

24. Bediako, D. K.; Rezaee, M.; Yoo, H.; Larson, D. T.; Zhao, S. Y. F.; Taniguchi, T.; Watanabe, K.; Brower-Thomas, T. L.; Kaxiras, E.; Kim, P., Heterointerface Effects in the Electrointercalation of van der Waals Heterostructures. *Nature* **2018**, 558, 425-429.

25. Ji, Z.; Hong, H.; Zhang, J.; Zhang, Q.; Huang, W.; Cao, T.; Qiao, R.; Liu, C.; Liang, J.; Jin, C.; Jiao, L.; Shi, K.; Meng, S.; Liu, K., Robust Stacking-Independent Ultrafast Charge Transfer in MoS_2/WS_2 Bilayers. *ACS Nano* **2017**, 11, 12020-12026.

26. Kim, C. O.; Kim, S.; Shin, D. H.; Kang, S. S.; Kim, J. M.; Jang, C. W.; Joo, S. S.; Lee, J. S.; Kim, J. H.; Choi, S. H.; Hwang, E., High Photoresponsivity in an All-Graphene p-n Vertical Junction Photodetector. *Nat. Commun.* **2014**, 5, 3249.

27. Zhang, X.; Liao, Q.; Liu, S.; Kang, Z.; Zhang, Z.; Du, J.; Li, F.; Zhang, S.; Xiao, J.; Liu, B.; Ou, Y.; Liu, X.; Gu, L.; Zhang, Y., Poly(4-Styrenesulfonate)-Induced Sulfur Vacancy Self-Healing Strategy for Monolayer MoS_2 Homojunction Photodiode. *Nat. Commun.* **2017**, 8, 15881.

28. Lee, S. Y.; Kim, U. J.; Chung, J.; Nam, H.; Jeong, H. Y.; Han, G. H.; Kim, H.; Oh, H. M.; Lee, H.; Kim, H.; Roh, Y. G.; Kim, J.; Hwang, S. W.; Park, Y.; Lee, Y. H., Large Work Function Modulation of Monolayer MoS_2 by Ambient Gases. *ACS Nano* **2016**, 10, 6100-6107.

29. Li, H. M.; Lee, D.; Qu, D.; Liu, X.; Ryu, J.; Seabaugh, A.; Yoo, W. J., Ultimate Thin Vertical p-n Junction Composed of Two-Dimensional Layered Molybdenum Disulfide. *Nat. Commun.* **2015**, 6, 6564.

30. Lim, J. Y.; Pezeshki, A.; Oh, S.; Kim, J. S.; Lee, Y. T.; Yu, S.; Hwang, D. K.; Lee, G. H.; Choi, H. J.; Im, S., Homogeneous 2D $MoTe_2$ p-n Junctions and CMOS Inverters Formed by Atomic-Layer-Deposition-Induced Doping. *Adv. Mater.* **2017**, 29, 1701798.

31. Seo, S.-Y.; Park, J.; Park, J.; Song, K.; Cha, S.; Sim, S.; Choi, S.-Y.; Yeom, H. W.; Choi, H.; Jo, M.-H., Writing Monolithic Integrated Circuits on a Two-Dimensional Semiconductor with a Scanning Light Probe. *Nat. Electron.* **2018**, 1, 512-517.

32. Liu, T.; Xiang, D.; Zheng, Y.; Wang, Y.; Wang, X.; Wang, L.; He, J.; Liu, L.; Chen, W., Nonvolatile and Programmable Photodoping in $MoTe_2$ for Photoresist-Free Complementary Electronic Devices. *Adv. Mater.* **2018**, 1804470.

33. Liu, Y.; Cai, Y.; Zhang, G.; Zhang, Y.-W.; Ang, K.-W., Al-Doped Black Phosphorus p-n Homojunction Diode for High Performance Photovoltaic. *Adv. Funct. Mater.* **2017**, 27, 1604638.

34. Thiruraman, J. P.; Fujisawa, K.; Danda, G.; Das, P. M.; Zhang, T.; Bolotsky, A.; Perea-Lopez, N.; Nicolai, A.; Senet, P.; Terrones, M.; Drndic, M., Angstrom-Size Defect Creation and Ionic Transport through Pores in Single-Layer MoS_2. *Nano Lett.* **2018**, 18, 1651-1659.

35. Bertolazzi, S.; Bonacchi, S.; Nan, G.; Pershin, A.; Beljonne, D.; Samori, P., Engineering Chemically Active Defects in Monolayer MoS_2 Transistors *via* Ion-

Beam Irradiation and Their Healing *via* Vapor Deposition of Alkanethiols. *Adv. Mater.* **2017**, 29, 1606760.

36. Ding, Q.; Czech, K. J.; Zhao, Y.; Zhai, J.; Hamers, R. J.; Wright, J. C.; Jin, S., Basal-Plane Ligand Functionalization on Semiconducting 2H-MoS_2 Monolayers. *ACS Appl. Mater. Interfaces* **2017**, 9, 12734-12742.

37. Amani, M.; Lien, D.-H.; Kiriya, D.; Xiao, J.; Azcatl, A.; Noh, J.; Madhvapathy, S. R.; Addou, R.; Santosh, K.; Dubey, M., Near-Unity Photoluminescence Quantum Yield in MoS_2. *Science* **2015**, 350, 1065-1068.

38. Lu, J.; Carvalho, A.; Chan, X. K.; Liu, H.; Liu, B.; Tok, E. S.; Loh, K. P.; Castro Neto, A. H.; Sow, C. H., Atomic Healing of Defects in Transition Metal Dichalcogenides. *Nano Lett.* **2015**, 15, 3524-3532.

39. Lin, P.; Zhu, L.; Li, D.; Xu, L.; Pan, C.; Wang, Z., Piezo-Phototronic Effect for Enhanced Flexible MoS_2/WSe_2 van der Waals Photodiodes. *Adv. Funct. Mater.* **2018**, 28, 1802849.

40. Li, P.; Jiang, C.; Xu, S.; Zhuang, Y.; Gao, L.; Hu, A.; Wang, H.; Lu, Y., *In Situ* Nanomechanical Characterization of Multi-Layer MoS_2 Membranes: From Intraplanar to Interplanar Fracture. *Nanoscale* **2017**, 9, 9119-9128.

41. Liu, K.; Zhang, L.; Cao, T.; Jin, C.; Qiu, D.; Zhou, Q.; Zettl, A.; Yang, P.; Louie, S. G.; Wang, F., Evolution of Interlayer Coupling in Twisted Molybdenum Disulfide Bilayers. *Nat. Commun.* **2014**, 5, 4966.

42. Tongay, S.; Suh, J.; Ataca, C.; Fan, W.; Luce, A.; Kang, J. S.; Liu, J.; Ko, C.; Raghunathanan, R.; Zhou, J.; Ogletree, F.; Li, J.; Grossman, J. C.; Wu, J., Defects

Activated Photoluminescence in Two-Dimensional Semiconductors: Interplay between Bound, Charged, and Free Excitons. *Sci. Rep.* **2013**, 3, 2657.

43. Chow, P. K.; Jacobs-Gedrim, R. B.; Gao, J.; Lu, T.-M.; Yu, B.; Terrones, H.; Koratkar, N., Defect-Induced Photoluminescence in Monolayer Semiconducting Transition Metal Dichalcogenides. *ACS Nano* **2015**, 9, 1520-1527.

44. Rivera, P.; Schaibley, J. R.; Jones, A. M.; Ross, J. S.; Wu, S.; Aivazian, G.; Klement, P.; Seyler, K.; Clark, G.; Ghimire, N. J.; Yan, J.; Mandrus, D. G.; Yao, W.; Xu, X., Observation of Long-Lived Interlayer Excitons in Monolayer $MoSe_2$-WSe_2 Heterostructures. *Nat. Commun.* **2015**, 6, 6242.

45. Zhu, J.; Wang, Z.; Yu, H.; Li, N.; Zhang, J.; Meng, J.; Liao, M.; Zhao, J.; Lu, X.; Du, L.; Yang, R.; Shi, D.; Jiang, Y.; Zhang, G., Argon Plasma Induced Phase Transition in Monolayer MoS_2. *J. Am. Chem. Soc.* **2017**, 139, 10216-10219.

46. Li, Y.; Cui, Q.; Ceballos, F.; Lane, S. D.; Qi, Z.; Zhao, H., Ultrafast Enterlayer Electron Transfer in Incommensurate Transition Metal Dichalcogenide Homobilayers. *Nano Lett.* **2017**, 17, 6661-6666.

47. Liu, Y.; Guo, J.; Zhu, E.; Liao, L.; Lee, S. J.; Ding, M.; Shakir, I.; Gambin, V.; Huang, Y.; Duan, X., Approaching the Schottky-Mott Limit in van der Waals Metal-Semiconductor Junctions. *Nature* **2018**, 557, 696-700.

48. Cheng, R.; Li, D.; Zhou, H.; Wang, C.; Yin, A.; Jiang, S.; Liu, Y.; Chen, Y.; Huang, Y.; Duan, X., Electroluminescence and Photocurrent Generation from Atomically Sharp WSe_2/MoS_2 Heterojunction p-n Diodes. *Nano Lett.* **2014**, 14, 5590-5597.

49. Liu, Y.; Wu, H.; Cheng, H.-C.; Yang, S.; Zhu, E.; He, Q.; Ding, M.; Li, D.; Guo,

J.; Weiss, N. O.; Huang, Y.; Duan, X., Toward Barrier Free Contact to Molybdenum Disulfide Using Graphene Electrodes. *Nano Lett.* **2015**, 15, 3030-3034.

50. Deng, Y.; Luo, Z.; Conrad, N. J.; Liu, H.; Gong, Y.; Najmaei, S.; Ajayan, P. M.; Lou, J.; Xu, X.; Ye, P. D., Black Phosphorus-Monolayer MoS_2 van der Waals Heterojunction p-n Diode. *ACS Nano* **2014**, 8, 8292-8299.

51. Li, M. Y.; Shi, Y.; Cheng, C. C.; Lu, L. S.; Lin, Y. C.; Tang, H. L.; Tsai, M. L.; Chu, C. W.; Wei, K. H.; He, J. H.; Chang, W. H.; Suenaga, K.; Li, L. J., Epitaxial Growth of a Monolayer WSe_2-MoS_2 Lateral p-n Junction with an Atomically Sharp Interface. *Science* **2015**, 349, 524-528.

52. Long, M.; Wang, P.; Fang, H.; Hu, W., Progress, Challenges, and Opportunities for 2D Material Based Photodetectors. *Adv. Funct. Mater.* **2018**, 1803807.

53. Du, J.; Liao, Q.; Hong, M.; Liu, B.; Zhang, X.; Yu, H.; Xiao, J.; Gao, L.; Gao, F.; Kang, Z.; Zhang, Z.; Zhang, Y., Piezotronic Effect on Interfacial Charge Modulation in Mixed-Dimensional van der Waals Heterostructure for Ultrasensitive Flexible Photodetectors. *Nano Energy* **2019**, 58, 85-93.

54. Si, H.; Kang, Z.; Liao, Q.; Zhang, Z.; Zhang, X.; Wang, L.; Zhang, Y., Design and Tailoring of Patterned ZnO Nanostructures for Energy Conversion Applications. *Sci. China Mater.* **2017**, 60, 793-810.

55. Li, H.; Tsai, C.; Koh, A. L.; Cai, L.; Contryman, A. W.; Fragapane, A. H.; Zhao, J.; Han, H. S.; Manoharan, H. C.; Abild-Pedersen, F.; Norskov, J. K.; Zheng, X., Activating and Optimizing MoS_2 Basal Planes for Hydrogen Evolution through the

Formation of Strained Sulphur Vacancies. *Nat. Mater.* **2016**, 15, 364.

56. Lee, J. U.; Woo, S.; Park, J.; Park, H. C.; Son, Y. W.; Cheong, H., Strain-Shear Coupling in Bilayer MoS_2. *Nat. Commun.* **2017**, 8, 1370.

57. Hu, Z.; Wu, Z.; Han, C.; He, J.; Ni, Z.; Chen, W., Two-Dimensional Transition Metal Dichalcogenides: Interface and Defect Engineering. *Chem. Soc. Rev.* **2018**, 47, 3100-3128.

58. Liang, L.; Zhang, J.; Sumpter, B. G.; Tan, Q. H.; Tan, P. H.; Meunier, V., Low-Frequency Shear and Layer-Breathing Modes in Raman Scattering of Two-Dimensional Materials. *ACS Nano* **2017**, 11, 11777-11802.

59. Lui, C. H.; Ye, Z. P.; Ji, C.; Chiu, K. C.; Chou, C. T.; Andersen, T. I.; Means-Shively, C.; Anderson, H.; Wu, J. M.; Kidd, T.; Lee, Y. H.; He, R., Observation of Interlayer Phonon Modes in van der Waals Heterostructures. *Phys. Rev. B* **2015**, 91, 165403.

60. van der Zande, A. M.; Kunstmann, J.; Chernikov, A.; Chenet, D. A.; You, Y.; Zhang, X.; Huang, P. Y.; Berkelbach, T. C.; Wang, L.; Zhang, F.; Hybertsen, M. S.; Muller, D. A.; Reichman, D. R.; Heinz, T. F.; Hone, J. C., Tailoring the Electronic Structure in Bilayer Molybdenum Disulfide *via* Interlayer Twist. *Nano Lett.* **2014**, 14, 3869-3875.

61. Chen, W.; Zhao, J.; Zhang, J.; Gu, L.; Yang, Z.; Li, X.; Yu, H.; Zhu, X.; Yang, R.; Shi, D.; Lin, X.; Guo, J.; Bai, X.; Zhang, G., Oxygen-Assisted Chemical Vapor Deposition Growth of Large Single-Crystal and High-Quality Monolayer MoS_2. *J. Am. Chem. Soc.* **2015**, 137, 15632-15635.

62. Huang, S.; Ling, X.; Liang, L.; Kong, J.; Terrones, H.; Meunier, V.; Dresselhaus, M. S., Probing the Interlayer Coupling of Twisted Bilayer MoS_2 Using Photoluminescence Spectroscopy. *Nano Lett.* **2014**, 14, 5500-5508.

63. Li, F.; Qi, J.; Xu, M.; Xiao, J.; Xu, Y.; Zhang, X.; Liu, S.; Zhang, Y., Layer Dependence and Light Tuning Surface Potential of 2D MoS_2 on Various Substrates. *Small* **2017**, 13, 1603103.

64. Zhang, Y.; Yan, X.; Yang, Y.; Huang, Y.; Liao, Q.; Qi, J., Scanning Probe Study on the Piezotronic Effect in ZnO Nanomaterials and Nanodevices. *Adv. Mater.* **2012**, 24, 4647-4655.

65. Zhang, Z.; Liao, Q.; Yu, Y.; Wang, X.; Zhang, Y., Enhanced Photoresponse of ZnO Nanorods-Based Self-Powered Photodetector by Piezotronic Interface Engineering. *Nano Energy* **2014**, 9, 237-244.

66. Wu, H.; Kang, Z.; Zhang, Z.; Zhang, Z.; Si, H.; Liao, Q.; Zhang, S.; Wu, J.; Zhang, X.; Zhang, Y., Interfacial Charge Behavior Modulation in Perovskite Quantum Dot-Monolayer MoS_2 0D-2D Mixed-Dimensional van der Waals Heterostructures. *Adv. Funct. Mater.* **2018**, 28, 1802015.

67. Wang, H.; Zhang, C.; Rana, F., Ultrafast Dynamics of Defect-Assisted Electron-Hole Recombination in Monolayer MoS_2. *Nano Lett.* **2015**, 15, 339-345.

68. Shi, H.; Yan, R.; Bertolazzi, S.; Brivio, J.; Gao, B.; Kis, A.; Jena, D.; Xing, H. G.; Huang, L., Exciton Dynamics in Suspended Monolayer and Few-Layer MoS_2 2D Crystals. *ACS Nano* **2013**, 7, 1072-1080.

69. Kresse, G.; Joubert, D., From Ultrasoft Pseudopotentials to the Projector

Augmented-Wave Method. *Phys. Rev. B* **1999**, 59, 1758-1775.

70. Kresse, G.; Furthmüller, J., Efficient Iterative Schemes Forab Initiototal-Energy Calculations Using a Plane-Wave Basis Set. *Phys. Rev. B* **1996**, 54, 11169-11186.

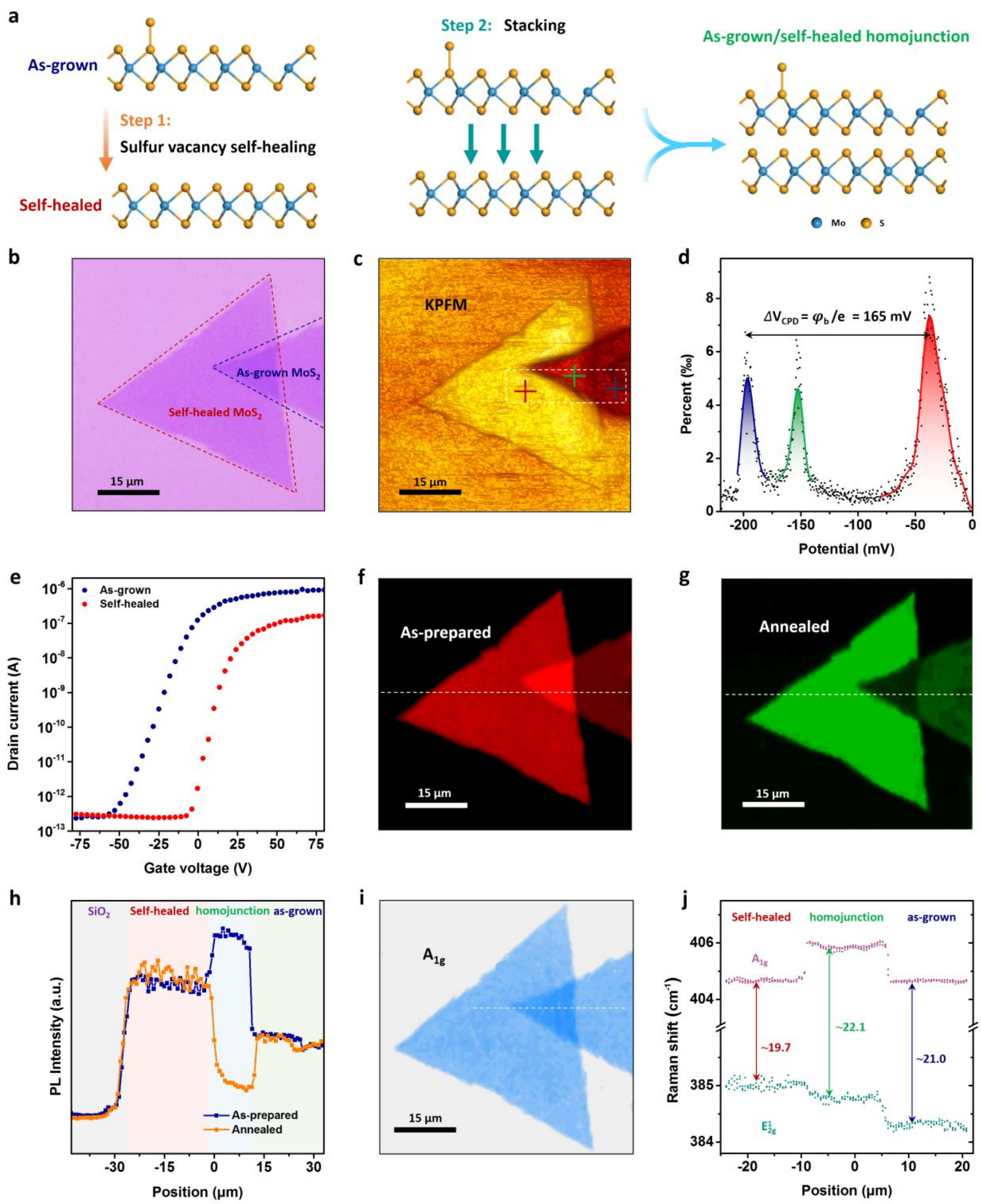

Figure 1. Construction of a MoS_2 vdW homojunction *via* sulfur vacancy self-healing. (a) The construction of MoS_2 homobilayers: one of the two as-grown MoS_2 monolayers

was used for sulfur vacancy self-healing and another one was stacked above the self-healed monolayer. (b) Optical microscopy (OM) image of the stacked MoS_2 homojunction. (c) Corresponding 2D surface potential image. (d) Work functions at the white dashed box shown in (c). The potential barrier between the as-grown and self-healed MoS_2 is ~165 meV. (e) Transfer characteristics of monolayer MoS_2 transistors before and after self-healing. (f, g) PL spectrum intensity mapping before (f) and after annealing (g). (h) PL spectrum intensities at the corresponding location of the white dashed lines shown in (f and g). (i) Corresponding Raman mapping constructed by integrating the A_{1g} mode of the as-prepared homojunction. (j) Raman peak statistics of E^1_{2g} and A_{1g} of the annealed homojunction at the corresponding location of the red dashed line shown in (i).

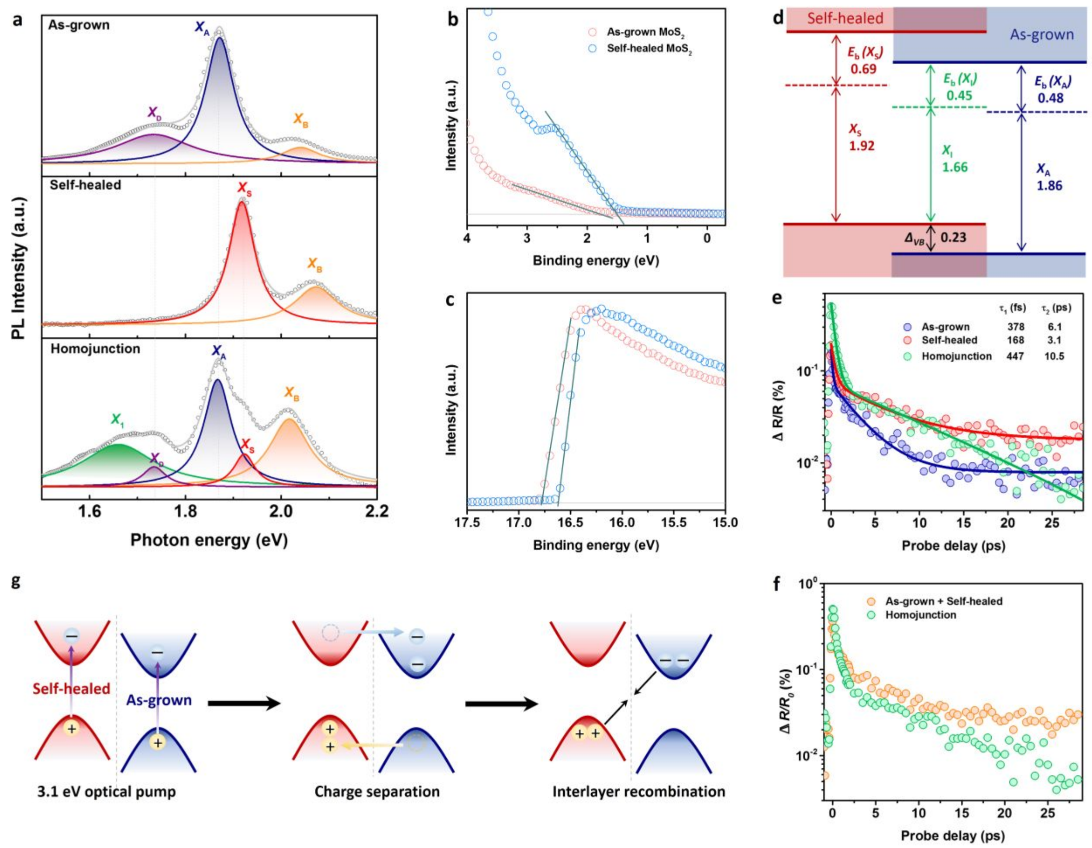

Figure 2. Interlayer charge transfer and Interlayer excitons of vdW MoS_2 homojunctions. (a) PL spectrums of the isolated monolayers and the homojunction at 77 K, and their Lorentzian deconvolutions. The orange, blue, red, purple and green lines represent the B exciton resonance peak (X_B), the A exciton resonance peak of the self-healed MoS_2 (X_S), the A peak exciton resonance of the as-grown MoS_2 (X_A), the defect peak of the sulfur vacancies (X_D) and the interlayer exciton peak of the homojunction (X_I), respectively. (b, c) Valence-band and secondary-edge spectrum of the as-grown and self-healed MoS_2. (d) Energy diagram showing the connection between the exciton transition energies, band offset and binding energies. E_b indicates the derived exciton binding energy, Δ_{VB} is the difference of the valence band maximum measured by UPS between the as-grown and self-healed film. (e) Differential reflection signal as a function of the probe delay measured from the as-grown, the self-healed and the

homojunction. The three lines indicate biexponential decay fits. (f) The signal of the MoS_2 homojunction and the simple signal sum of the two isolated as-grown and self-healed monolayers. (g) Schematic illustration of charge separation processes in the homojunction. After the 3.1 eV pump excitation, electrons (holes) are rapidly transferred in the as-grown (self-healed). Then the intralayer recombination was measured by setting the probe photon energy of 1.91 eV.

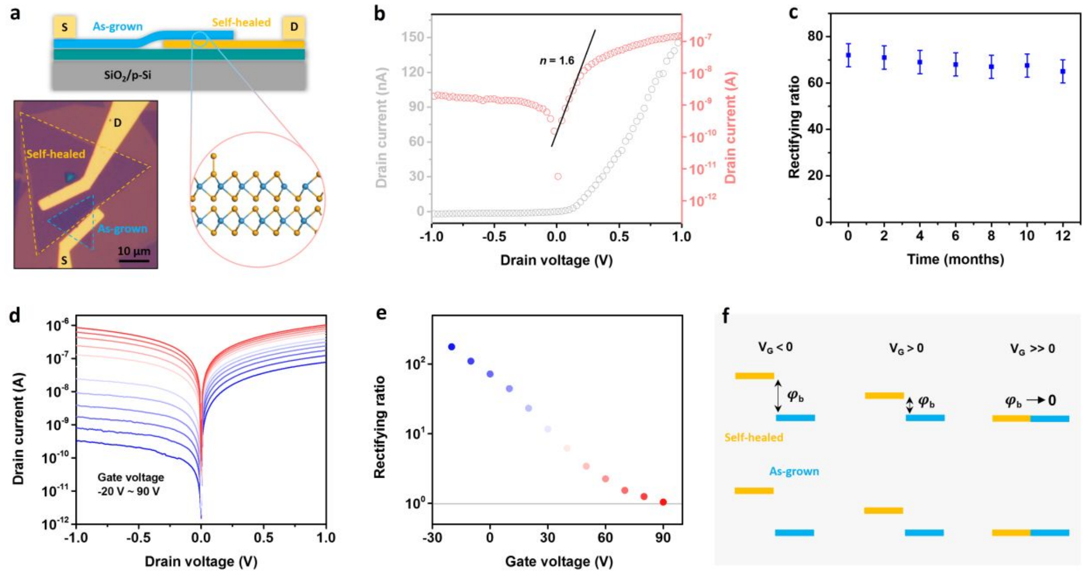

Figure 3. Current rectifying effect of MoS_2 homojunction photodiodes. (a) Schematic diagram of a MoS_2 homojunction device on SiO_2/Si substrate with Au electrodes. Inset is the OM image of the device. (b) Output characteristic on linear (orange) and logarithmic (blue) scale of the MoS_2 homojunction. (c) Rectifying ratio of the homojunction measured during 12 months of storage under ambient conditions. (d) The output characteristic of the MoS_2 homojunction under different back gate voltage V_G. (e) The rectification ratio under different gate voltage. (f) Energy band structure under different gate voltage.

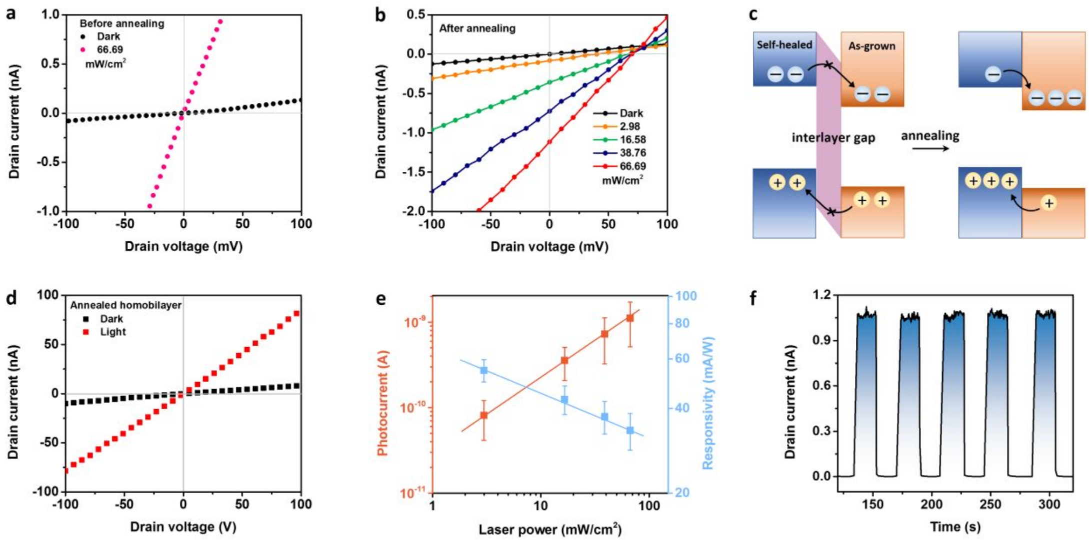

Figure 4. Photovoltaic effect of MoS_2 homojunction photodiodes. (a, b) Output characteristic of the homojunction at dark and under light illumination both before (a) and after (b) annealing. With the decrease of laser power intensity, both short-circuit current and open-circuit voltage will decrease in (b). (c) Schematic of photocurrent generation processes under light illumination for the as-prepared (left) and annealed (right) interfaces. (d) Output characteristic of the as-grown/as-grown homobilayer at dark and under light illumination. (e) Photocurrent and responsivity calculated as a function of laser power at zero voltage. The photocurrent increase and the responsivity decrease as the power increases. (f) Photocurrent response of the photodiode at zero voltage (66.69 mW/cm^2).

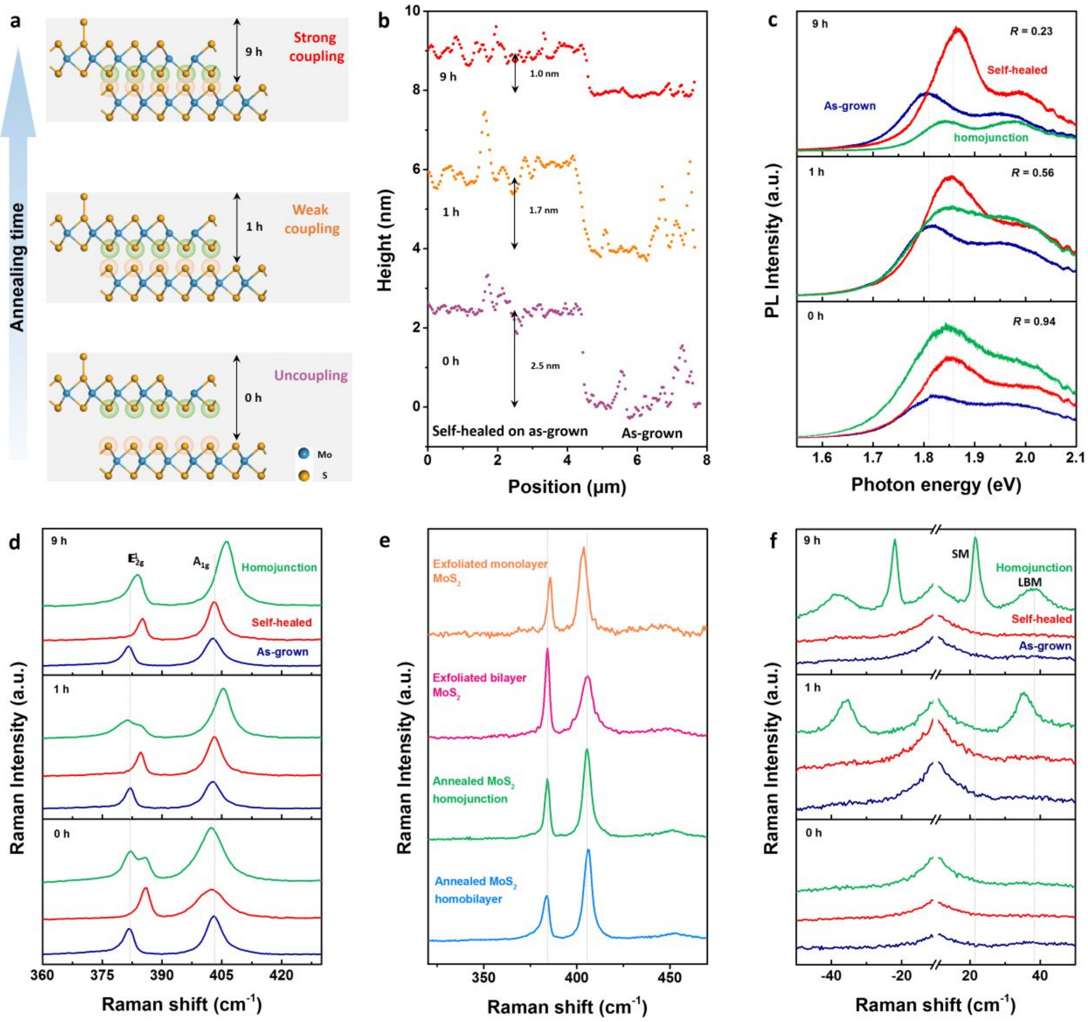

Figure 5. Formation mechanism of strong coupling interface. (a) Schematic of annealing enhanced interlayer coupling effect. (b) Cross-sectional height profiles of a self-healed monolayer on the as-grown monolayer for different annealing time. (c) PL and (d) Raman spectrums for the as-grown MoS_2, the self-healed MoS_2 and the homojunction in the different annealed conditions, for the same sample. *R* indicates the PL spectrum intensity ratio of the homojunction and the sum of the as-grown and self-healed MoS_2. (e) Raman spectrums of the exfoliated MoS_2 monolayer, the exfoliated MoS_2 bilayer, the annealed MoS_2 homojunction and the annealed as-grown/as-grown MoS_2 homobilayer.

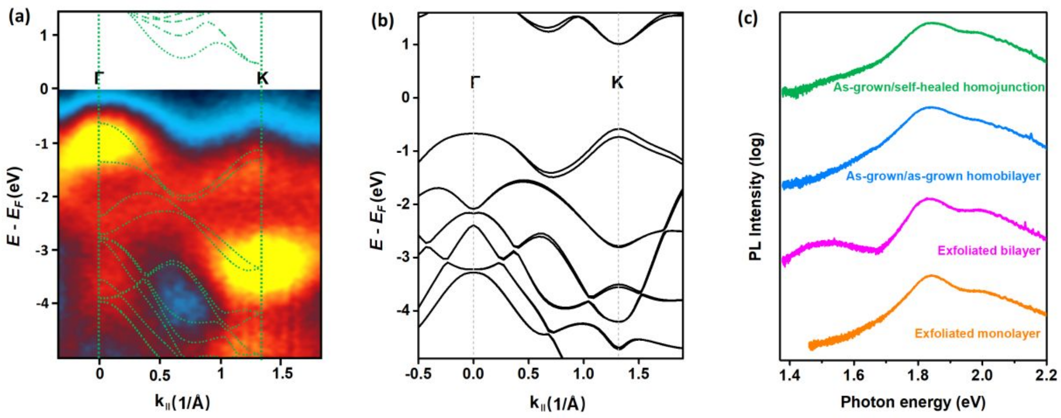

Figure 6. Electronic structure of MoS_2 homojunctions. (a) Experimental band structures of the MoS_2 homojunction measured by ARPES, shown as momentum slice along Γ-K. The green dashed lines correspond to the theoretical band structures calculated by DFT. The band edges of Γ point of the MoS_2 homojunction is higher than those of K point, indicating that the homojunction possesses strong-coupled interface, and is also an indirect bandgap junction. (b) Theoretical band structures of MoS_2 monolayer. (c) PL spectrums of the annealed MoS_2 homojunction, the annealed MoS_2 homobilayer, the exfoliated MoS_2 bilayer, and the exfoliated MoS_2 monolayer. Sulfur vacancies in MoS_2 homojunction and homobilayer will impede the detection of the indirect exciton peak.

Table 1. Interlayer coupling strength comparison of the stacked MoS_2 homojunction and vdW heterostructures.

Device	LBM (cm^{-1})	SM	A_{1g} - E^1_{2g} (cm^{-1})	E_K - E_Γ (eV)	Reference
MoS_2 homojunction	~38.5	Yes	~22.1	Negative	**This work**
MoS_2 homobilayer	32-39	Yes	21-22	Negative	Ref.[59]
Natural bilayer MoS_2	~41	Yes	22-24	Negative	Ref.[56]
$MoSe_2$/WSe_2	/	/	/	Positive	Ref.[21]
MoS_2/WSe_2	~32	No	/	Positive	Ref.[59]
LBM: layer-breathing mode. SM: shear mode.					

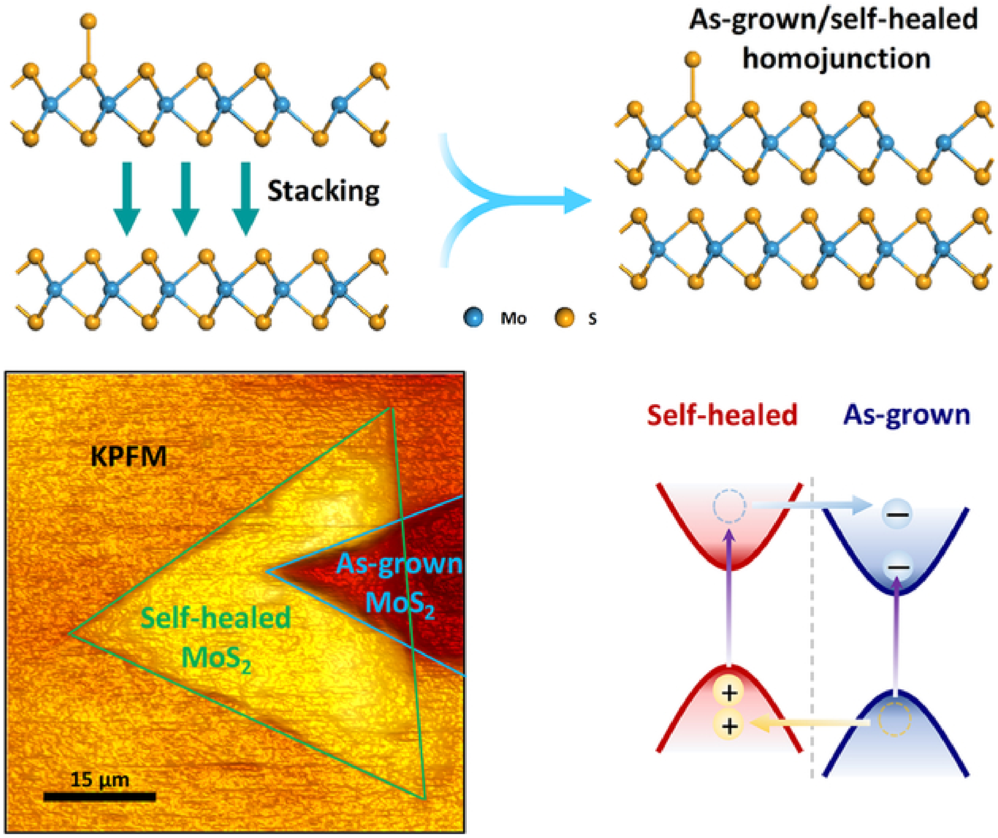

Table of Contents

53x44mm (300 x 300 DPI)